Structural effects on the emission properties of Pr3+-doped Ba2NaNb5O15 crystals

Enrico Cavalli, Gianluca Calestani, Francesco Mezzadri, Raffaele Faoro, Mauro Tonelli, Philippe Boutinaud

Structural effects on the emission properties of Pr^{3+}-doped $Ba_2NaNb_5O_{15}$ crystals

Enrico Cavalli[1,*], Gianluca Calestani[1], Francesco Mezzadri[1], Raffaele Faoro[2], Mauro Tonelli[2] and Philippe Boutinaud[3]

[1] Dipartimento di Chimica Generale ed Inorganica, Chimica Analitica, Chimica Fisica, Università di Parma, Parma, Italy.

[2] NEST-Istituto di Nanoscienze-CNR, Dipartimento di Fisica, Università di Pisa, Pisa, Italy.

[3] Clermont Université, ENSCCF, Laboratoire des Matériaux Inorganiques, BP10448, F-63000 Clermont-Ferrand, France.

* Corresponding author. E-mail address: enrico.cavalli@unipr.it

Abstract. Single crystals of $Ba_2NaNb_5O_{15}$ doped with Pr^{3+} have been grown from sodium tetraborate flux. Their emission properties have been measured as a function of the doping level under different excitation and temperature conditions. The experimental observations have been accounted for by considering the effects of the crystal structure, of the doping mechanisms and of the interactions between host lattice and doping ions. The proposed conclusions have been verified by means of single crystal X-ray diffraction measurements and the resulting site occupancies of the active ions have been discussed in the light of the synthesis procedure.

PACS: 78.55.Hx; 61.66.Fn

1. Introduction

$Ba_2NaNb_5O_{15}$ (BNN) belongs to the family of the niobates with the tungsten bronze (TB) structure. These compounds have attractive photorefractive, ferroelectric and non linear optical properties [1]. BNN is also an interesting host material for luminescent ions. Nd^{3+}-doped crystals have been investigated in order to develop self doubling laser media [2, 3]. Studies extended to BNN activated with Yb^{3+} [4], Er^{3+} [5], Tm^{3+} and Ho^{3+} [6, 7] have confirmed its potentialities as host lattice for laser ions. We have recently explored the visible emission properties of BNN crystals activated with Eu^{3+}, Dy^{3+}, Tb^{3+} and Sm^{3+} [8], pointing out the issues concerning the site occupancy in this host lattice and the analogies with SBN:Ln^{3+} (Ln^{3+}= rare earth ions). In this paper we thoroughly investigate the emission properties of Pr^{3+}-doped BNN (hereafter Pr:BNN) crystals as a function of the temperature, of the doping concentration and of the excitation conditions. Our interest in this system is related to different interconnected aspects: the development of a new visible emitting material, the analysis of its excited states dynamics and of the interactions between optical centres and lattice constituents in the light of the structural properties of the host and of the Pr^{3+} site occupancy, the possibility of extending the obtained information to other members of the TB niobate family, and so on.

2. Experimental

2.1 Crystal growth.

Single crystals of BNN singly doped with Pr^{3+} were grown by means of the flux growth method. Pure BaO, Nb_2O_5 and $Na_2B_4O_7$ were used as starting materials. The doping ions were added as Pr_6O_{11} with nominal 0.5%, 2% and 8% molar ratios with respect to Ba. The starting mixture was placed in a Pt crucible and heated to melt (1250 °C) in a horizontal furnace. After a 12 h soaking time, the temperature was slowly lowered (2-3 °C/h) to 400 °C, then the furnace was turned off. Crystals with size up to of $2\times2\times3$ mm^3 and of sufficient optical quality were separated from the flux by dissolving it in hot diluted HCl. The structural properties of the grown crystals will be discussed in details in Sect. 4. For the moment it is sufficient to point out that the incorporation of Pr^{3+} ions into the BNN lattice requires charge compensation that, combined with

the intrinsic disorder of the TTB structure, results in the formation of different non equivalent optical centers and then in a significant inhomogeneous broadening of the absorption and emission features.

2.2 Characterization.
Single crystal X-ray diffraction (XRD) data were collected on a modified Philips PW1100 single crystal diffractometer using graphite monochromatized Mo Kα radiation. Experimental details are reported in Table 1.
The room temperature emission and excitation spectra were measured using a Fluoromax-3 (Jobin-Yvon) spectrofluorimeter. The low temperature spectra were measured in the 485-760 nm range by using an Argon laser in single-line configuration to pump the $^3P_0$ manifold. The crystal was mounted on the cold finger of a closed-cycle He cryocooler. The luminescence was chopped and focused by a 75 mm focal lens on the input slit of a D330 Hillger & Watts monochromator with 300 mm focal length (resolution: 0.1 nm), processed by a lock-in amplifier and revealed by means of a S20 photomultiplier. A Glan-Thomson prism was placed at the entrance slit of the monochromator in order to perform polarized measurements. The decay time measurements were carried out upon 445 nm excitation by means of the second harmonic of tunable Ti-Sa pulsed laser (pulse duration ~ 30 ns, repetition rate 10Hz).

3. Luminescence spectroscopy

3.1. 10 K emission spectra.
The 10 K polarized emission spectra of 0.5%, 2% and 8% Pr:BNN measured upon 476.5 nm CW laser excitation are shown in figure 1. They are composed of four emission manifolds: the intense $^3P_0 \rightarrow {}^3H_4$ transition at 495 nm, the weak $^3P_0 \rightarrow {}^3H_5$ multiplet at around 550 nm, a complex band system in the 600-670 nm range, including the $^1D_2 \rightarrow {}^3H_4$ (~605 nm), $^3P_0 \rightarrow {}^3H_6$ (610-650 nm) and $^3P_0 \rightarrow {}^3F_2$ (650-670 nm) transitions, and the weak $^3P_0 \rightarrow {}^3F_{3,4}$ emission at around 750 nm.

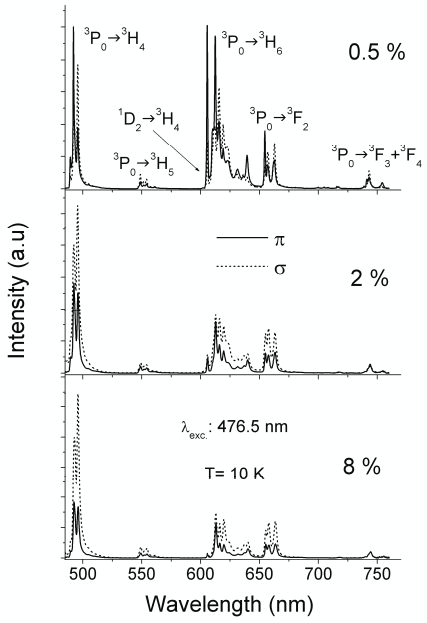

Figure 1. Polarized emission spectra measured upon 476.5 nm laser excitation.

The intensity ratio between the observed manifolds as well as the polarization behaviour of their components change with the doping level. This in our opinion is the consequence of the presence of different (and interacting) optical centres whose relative concentrations vary with the total Pr^{3+} content independently one from the other. As expected, all features are inhomogeneously broadened, the sharpest ones having FWHM (full width at half maximum) values of the order of 30-40 cm^{-1}. The broadness of the emission features

depend on the excitation wavelength: as an example, Figure 2 (a) compares the 600-670 nm manifold measured upon 476.5 and 458 nm laser excitation. The latter is significantly broader, indicating that the 458 nm radiation excites a number of non-equivalent centres larger than that excited by the 476.5 nm one. It is clear from in figure 2 (b) that that the relative intensity of the $^1D_2 \rightarrow {}^3H_4$ emission transition strongly decreases with the doping level. This is an expected result, since the emission properties of Pr^{3+}-doped compounds are significantly affected by the activator concentration. In the case of the $^3P_0$ level the concentration quenching is ascribed to cross relaxation processes of the type [9]:

$$[{}^3P_0, {}^3H_4] \rightarrow [{}^1G_4, {}^1G_4] \qquad \text{(i)}$$
$$[{}^3P_0, {}^3H_4] \rightarrow [{}^1D_2, {}^3H_6] \qquad \text{(ii)}$$

shown in Fig. 3(a).

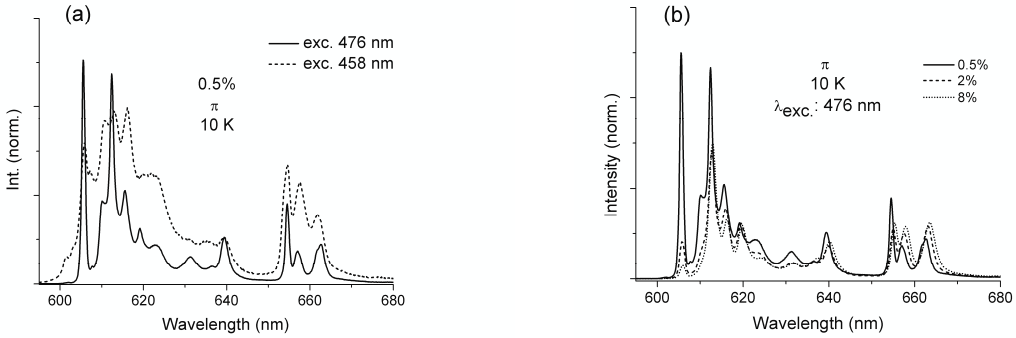

Figure 2. The 600-680 nm emission manifold (π polarization) measured for different excitation wavelengths (a) and Pr^{3+} concentrations (b).

Process (i) is not resonant, since the two involved transitions occur at energies differing by about 950 cm^{-1}, and process (ii) is nearly but not fully resonant. In consequence, both are expected to be favoured by phonon assistance, since phonons of suitable energy are available in the IR or Raman spectrum [10]. This mechanism is concomitant with the $^3P_0 \rightarrow {}^1D_2$ multiphonon relaxation. The cross relaxation involving the $^1D_2$ state (figure 3 (b)):

$$[{}^1D_2, {}^3H_4] \rightarrow [{}^1G_4, {}^3F_4] \qquad \text{(iii)}$$

is in practice a resonant process, then we have to expect a strong concentration and a weak temperature dependence. In addition to these processes, the mechanism involving charge transfer states have to be considered.

3.2. 298 K emission spectra.

As the temperature increases the emission bands broaden and their intensity decreases. At 300 K the spectra present a broad luminescence in the 600-660 nm range, with two components: the more intense (composed by the $^1D_2 \rightarrow {}^3H_4$ and $^3P_0 \rightarrow {}^3H_6$ transitions) has maximum at 605 nm that shifts to 620 nm as with concentration increasing as a consequence of the quenching of the $^1D_2$ emission, the minor one ($^3P_0 \rightarrow {}^3F_2$) peaks at 655 nm (Fig. 4 (a)). The relative intensities of the spectral components depend on the excitation wavelength: this is a typical consequence of the presence of the IVCT state that favours the population of the $^1D_2$ state. The spectrum of the diluted crystal is rather similar to that reported for SBN:Pr (1%) [11], indicating similar environments for the optically active ions in the two lattices. The excitation spectrum (Fig. 4 (b)) is characterized by three band systems located in the 420-500, 340-410 and <300 nm regions. The last one corresponds to the host absorption band feeding the Pr^{3+} emission through an energy transfer process. The manifold in the blue region, resolved into three well separated components, is ascribed to the $^3H_4 \rightarrow {}^3P_J$ (J= 0, 1,2), $^1I_6$ absorption of Pr^{3+}. The band located in the 340-410 nm range is to low in energy to be assigned to a $4f^2 \rightarrow 4f^15d^1$ transition and it is ascribed to the intervalence charge transfer (IVCT) process:

$$Pr^{3+}+Nb^{5+}\rightarrow Pr^{4+}+Nb^{4+}$$

already observed in Pr^{3+}-doped niobates [12]. It is interesting to note that the IVCT maximum shifts to higher energy as the doping level increases: it is located at 374 nm in the 0.5% case, at 368 nm in the 2% and at 345 nm in the 8% case. As pointed out by Boutinaud et al. [12], the position of the IVCT state is related to the optical electronegativity of the involved transition metal ion (Nb^{5+} in the present case) and to its minimum distance with respect to the lanthanide ion.

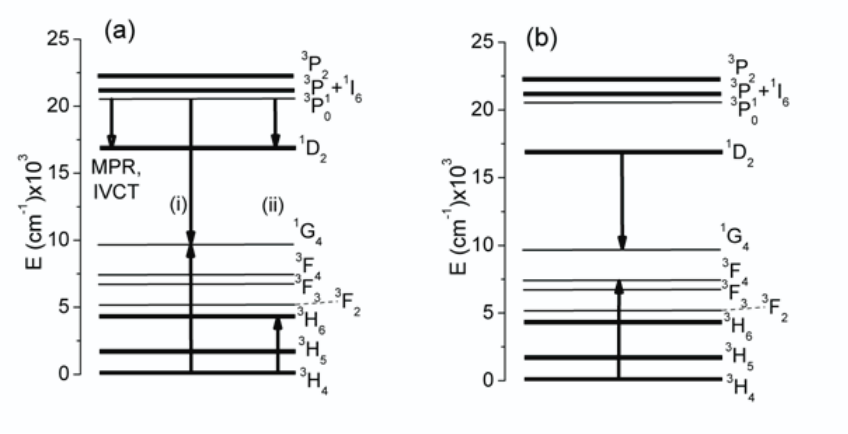

Figure 3. Non radiative mechanisms affecting the $^3P_0$ (a) and $^1D_2$ (b) emission of Pr^{3+} in oxide lattices.

This dependence is formalized by the empirical equation:

$$IVCT(\mathrm{Pr}^{3+}, cm^{-1}) = 58800 - 49800\frac{\chi_{opt}\left(M^{n+}\right)}{d(\mathrm{Pr}^{3+} - M^{n+})} \qquad (1)$$

where $\chi_{opt}\left(M^{n+}\right)$ is the optical electronegativity of the closed-shell transition metal ion M^{n+} and $d(Pr^{3+}$ - $M^{n+})$ is the shortest interatomic distance between Pr^{3+} and M^{n+}. In the diluted crystals the shortest Pr^{3+}-Nb^{5+} distance calculated using eq. (1) is 2.89 Å. In the BNN lattice however, Pr^{3+} is expected to replace Na^+ (A_2 site) or Ba^{2+} (A_1 site). In both cases the shortest Pr^{3+}-Nb^{5+} distances, 3.36 and 3.60 Å respectively, are not consistent with the calculated value. Only in the case of C site occupancy the resulting distance, 2.90 Å, is practically coincident with the evaluated one.

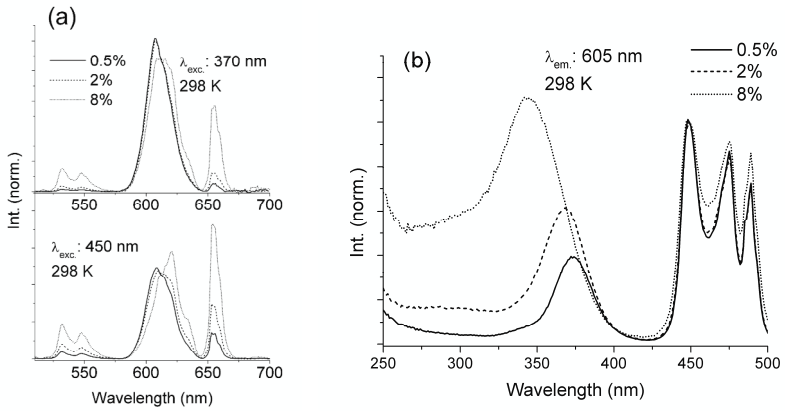

Fig. 4. Room temperature unpolarized emission (a) and excitation (b) spectra of Pr:BNN.

In addition, the IVCT shift with increasing Pr^{3+} concentration indicates that the average shortest Pr^{3+}-Nb^{5+} distance increases with the doping level. These are unexpected and interesting issues that we have decided to investigate in more details by XRD techniques.

Table 1. Crystal data and refinement parameters

Compound	Pr:BNN (0.5%)	Pr:BNN (2%)	Pr:BNN (8%)
Formula weight	998.92	999.12	998.67
Crystal habit	needle	needle	needle
Crystal colour	colorless	colorless	colorless
Crystal dimensions, mm	0.53 x 0.07 x 0.05	0.41 x 0.07 x 0.07	0.50 x 0.08 x 0.08
Crystallographic system	tetragonal	tetragonal	tetragonal
Space group	P4bm	P4bm	P4bm
Cell parameters:			
a, Å	12.465(5)	12.464(4)	12.463(4)
c, Å	3.986(2)	3.986(2)	3.984(2)
α, °	90	90	90
β, °	90	90	90
γ, °	90	90	90
V, $Å^3$	619.3(5)	619.2(4)	618.8(4)
Z	2	2	2
D_{calc}, Mg m^{-3}	5.357	5.359	5.360
Linear abs. coefficient, cm^{-1}	10.784	10.818	10.865
Absorpt. correction type	ψ-scan	ψ-scan	ψ-scan
Absorpt. correction T_{max}	0.411	0.468	0.421
Absorpt. correction T_{min}	0.576	0.404	0.351
Temperature, K	293	293	293
Radiation, Å	0.71073	0.71073	0.71073
2θ range, °	3.27-35.01	3.27-35.01	3.27-45.02
Total measured reflections	2974	2976	5473
Unique reflections	802	804	1451
Unique observed reflection	792	740	1212
Criterion for obs. reflections	I>2σ(I)	I>2σ(I)	I>2σ(I)
Reflections used (NO) [a]	802	804	1451
Refined parameters (NV)	64	66	66
NO/NV ratio	12.53	12.18	21.98
$R = \Sigma \lvert \Delta F \rvert / \Sigma \lvert F_o \rvert$ [b]	0.0274	0.0238	0.0439
$wR2 = [\Sigma w \lvert \Delta F^2 \rvert^2 / \Sigma w \lvert Fo^2 \rvert^2]^{½}$ [c]	0.0664	0.0575	0.0999
$GOF=[\Sigma w \lvert \Delta F^2 \rvert^2 / (NO-NV)]^{½}$	0.998	1.132	1.007
Flack parameter	0.08(6)	0.09(6)	0.04(6)
Extinction coefficient	0.0154(9)	0.0092(5)	0.0091(10)
Maximum shift/esd, last cycle	0.002	0.001	0.04
Maximum residual peak, e/$Å^3$	1.50	1.98	2.06

[a] Refinement based on the reflections with $I > 0$.
[b] Calculated on the observed reflections.
[c] Calculated on the reflections used in the refinement.

3.3 Decay time measurements

The emission kinetics of both $^3P_0$ (655 nm) and $^1D_2$ (605 nm) states have been measured at different temperatures upon 455 nm excitation (Fig. 5). The profile of the $^3P_0$ emission is a single exponential only in the case of the diluted sample at 10 K. As the temperature and/or the concentration increases the curves significantly deviates from the exponential behaviour. Possible reasons of this effect can be:

I. as the concentration increases the distribution of the Pr^{3+} ions among the different sites tend to vary, as well as the effect of the related charge compensation mechanisms.
II. the $^3P_0 \rightarrow {}^1D_2$ multiphonon relaxation process requires at least four high energy (840 cm^{-1}) host phonons to occur, since the gap between the involved levels is of the order of 3300-3500 cm^{-1}. It then constitutes a temperature dependent contribution to the $^3P_0$ depopulation.
III. the temperature dependent cross relaxation mechanisms.
IV. the de-excitation through the IVCT state can be favoured by suitable phonon assistance and then could have some temperature dependence.

It is clearly impossible to analyze the profiles on the basis of a single reliable model. We have then evaluated the effective emission decay times using the eq (2) [13]:

$$\tau = \frac{\int t \cdot I(t)dt}{\int I(t)dt} \qquad (2)$$

where $I(t)$ represents the luminescence intensity at time t. The obtained values, reported in Fig. 5 in proximity of the corresponding curves, evidence a relatively small variability, despite the number of processes potentially involved.

The 10 K $^1D_2$ profiles are characterized by a risetime, approximately of the order of 1 μs, confirming the feeding from the $^3P_0$ upper level through the II-IV processes above mentioned. At 298 K the risetime disappears because the above mentioned temperature dependent relaxation processes from $^3P_0$ become much more effective and the feeding process faster. The decays are non exponential in consequence of the presence of non equivalent optical centres. The values of the effective decay times, calculated with eq. (2), reveal a strong concentration dependence compatible with the resonant character of the $[^1D_2, {}^3H_4] \rightarrow [^1G_4, {}^3F_4]$ cross relaxation responsible of the non radiative depopulation of the $^1D_2$ level.

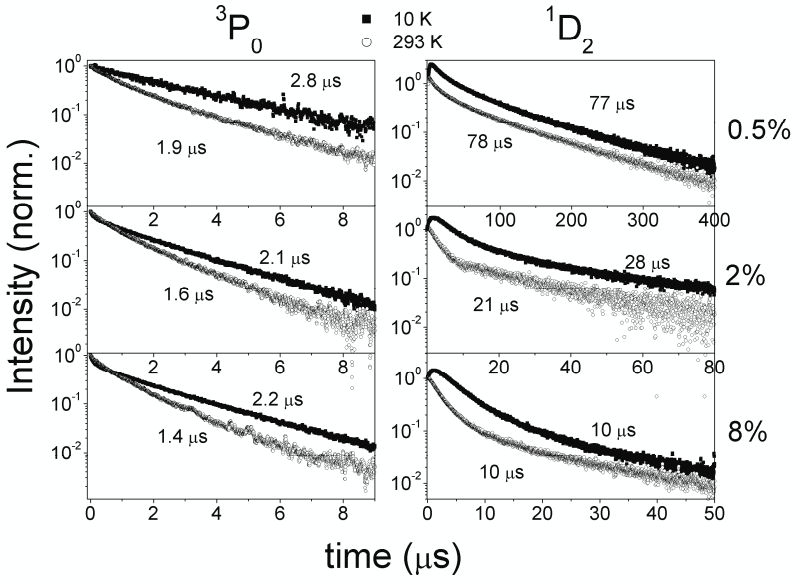

Fig. 5. Emission decay profiles of Pr:BNN.

4. Structural characterization

Three single crystals with nominal Pr/Ba ratios 0.5%, 2% and 8% were characterized by single crystal XRD. Crystal data are very similar, as reported in Table 1, and consistent with the typical tetragonal tungsten bronze (TTB) structure, characterized by the structural formula $(A_1)_x(A_2)_yC_zB_{10}X_{30}$, where *x* can ideally vary in the 0-2 range and *y, z* in the 0-4 range. The typical framework (Fig. 6) can be thought as derived from the perovskite structure by rotation of some $[BX_6]$ polyhedra and is formed by corner sharing $[BX_6]$ octahedral units whose linking produces three different types of channels (also called tunnels) containing the extra-framework cations in A_1, A_2, and C sites, respectively. In terms of coordination polyhedra, the A_2 cations are 15-fold coordinated in the tunnel with a pentagonal section, the A_1 cations are 12-fold coordinated in the surviving perovskite cage, and the C cations are 9-fold coordinated in channels characterized by a triangular section. In our case the structure was solved with SIR2002 [14] and refined with SHELX97 [15].

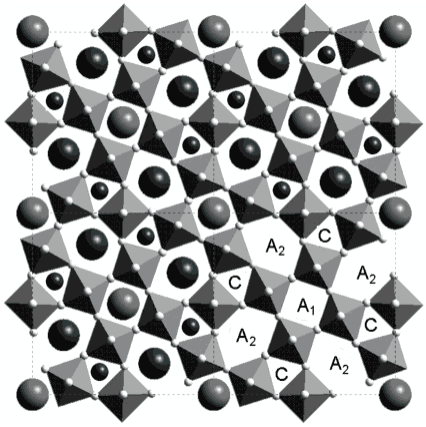

Figure 6. TTB structure with the conventional sites nomenclature.

After a preliminary structure refinement in which only the presence of Ba^{2+} and Na^{+} (located in A_2 and A_1, respectively) as extra-framework cations was taken into account, difference Fourier maps revealed in all cases a residual electron density in the triangular channels, suggesting a partial cationic occupation of the corresponding C sites. Since these residuals were not detected in undoped BNN crystals previously characterized, a possible site occupation by praseodymium was considered. Owing to the reduced cage dimension, this hypothesis could appear quite rash, unless to evaluate carefully the local effects produced by structural modulation. In fact TTB structures, known for a great number of oxides and fluorides, are usually characterized in the low temperature region of the phase diagram (very often extending well above RT) by a typical structural modulation along the [110] crystallographic direction, ranging from incommensurate to commensurate depending on chemical composition and connected to the doubling of the *c* parameter (≈ 8 Å). The structural modulation, ascribed to the existence of a cooperative tilt of the $[NbO_6]$ octahedra that reduces the real symmetry from tetragonal to orthorhombic, is at the basis of ferroelasticity in these systems.

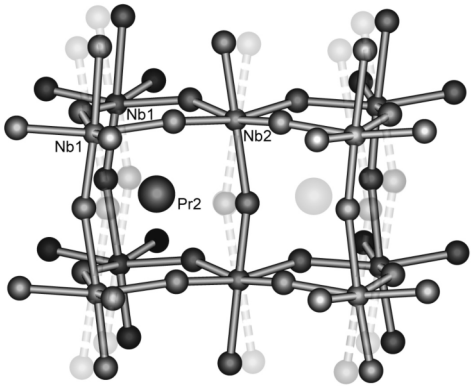

Fig. 7. Configurations of the triangular channels resulting from the modulation of the BNN structure and allowing the accommodation of the Pr^{3+} ions in the C site.

The fundamental averaged structure of BNN at room temperature was determined at the end of the 1960s by Jamieson et al.[16].

Table 2. Atomic coordinates and displacement parameters ($Å^2$).

Pr:BNN (0.5%)

atom	site multiplicity	x	y	z	U_{eq}	site occupancy
Nb2	2	0.0000	0.5000	0.5000	0.00457(17)	1
Nb1	8	0.07404(3)	0.20942(3)	0.4994(6)	0.00176(13)	1
Ba2	8	0.3357(3)	0.1787(3)	0.0132(6)	0.0115(7)	0.4845(13)
Na1	2	0.0000	0.0000	0.007(3)	0.0074(7)	1
Pr2	4	0.1128(15)	0.3872(15)	0.051(7)	0.010	0.0183(16)
O1	8	-0.0064(3)	0.3437(3)	0.546(3)	0.0173(14)	1
O2	4	0.2160(3)	0.2840(3)	0.536(3)	0.0081(13)	1
O3	8	0.1410(4)	0.0698(3)	0.558(2)	0.0193(15)	1
O41	8	0.0914(10)	0.1952(9)	0.033(5)	0.0230(19)	0.50
O42	8	0.0572(10)	0.2150(10)	0.044(4)	0.0230(19)	0.50
O5	4	0.0141(7)	0.4859(7)	0.018(8)	0.020(3)	0.50

Pr:BNN (2%)

atom	site multiplicity	x	y	z	U_{eq}	site occupancy
Nb2	2	0.0000	0.5000	0.5000	0.00531(15)	1
Nb1	8	0.07410(3)	0.20939(3)	0.4971(6)	0.00217(11)	1
Ba2	8	0.3365(2)	0.1793(2)	0.0103(7)	0.0105(5)	0.4809(12)
Na1	2	0.0000	0.0000	0.001(3)	0.0175(12)	0.970(4)
Pr1	2	0.0000	0.0000	0.001(3)	0.0175(12)	0.031(4)
Pr2	4	0.1162(19)	0.3838(19)	0.054(9)	0.010	0.0131(14)
O1	8	-0.0063(3)	0.3438(3)	0.544(3)	0.0172(13)	1
O2	4	0.2163(3)	0.2837(3)	0.536(3)	0.0073(13)	1
O3	8	0.1414(3)	0.0698(3)	0.555(2)	0.0192(15)	1
O41	8	0.0904(9)	0.1959(9)	0.025(6)	0.0258(19)	0.50
O42	8	0.0584(9)	0.2153(9)	0.033(5)	0.0258(19)	0.50
O5	4	0.0144(6)	0.4856(6)	0.023(6)	0.016(3)	0.50

Pr:BNN (8%)

atom	site multiplicity	x	y	z	U_{eq}	site occupancy
Nb2	2	0.0000	0.5000	0.5000	0.00611(12)	1
Nb1	8	0.07395(2)	0.20972(2)	0.5031(5)	0.00527(8)	1
Ba2	8	0.33566(16)	0.17868(17)	0.0146(5)	0.0139(4)	0.4720(10)
Na1	2	0.0000	0.0000	0.007(2)	0.0138(7)	0.920(4)
Pr1	2	0.0000	0.0000	0.007(2)	0.0138(7)	0.080(3)
Pr2	4	0.112(2)	0.388(2)	-0.025(15)	0.010	0.0084(13)
O1	8	-0.0065(3)	0.3436(3)	0.542(3)	0.0275(18)	1
O2	4	0.2162(3)	0.2838(3)	0.540(4)	0.017(2)	1
O3	8	0.1404(3)	0.0691(3)	0.554(4)	0.036(3)	1
O41	8	0.0909(8)	0.1962(8)	0.037(5)	0.0280(17)	0.50
O42	8	0.0568(8)	0.2139(8)	0.037(5)	0.0280(17)	0.50
O5	4	0.0131(6)	0.4869(6)	0.044(5)	0.020(3)	0.50

The first attempt to describe the modulated structure was made by Lin and Bursill [17] on the basis of electron diffraction (ED) data in an orthorhombic supercell with $a \approx b \approx 2\ a_{TTB}\sqrt{2}$, $c = 2\ c_{TTB}$ and space group *Im*2*a*. Further studies on de-twninned crystals by Labbe´ et al. [18] demonstrated that the supercell describing the quasi-commensurate modulation is in reality half in volume, being $b \approx a_{TTB}\sqrt{2}$, and its symmetry is consistent with the *Bbm*2 space group.The results of Labbé were then confirmed by Fabbrici et al. [19] for $K_{0.525}FeF_3$ and by Mezzadri et al. [20] for $K_{0.6}FeF_3$, confirming this modulation as generally distinctive of TTB phases and not only of BNN. The use of de-twninned crystals revealed to be fundamental in structural studies of BNN, where ferroelastic domains connected to the exchange of the *a* and *b* axes of the superstructure occurs on a scale that is below the coherence length of X-ray, so that the modulation satellites are usually observed only by electron diffraction (ED). In spite of the typical absence of modulation satellites, the existence of the structural modulation leaves a characteristic trace in single crystal XRD data, consisting in an anomalous elongation of the anisotropic displacement parameters (a.d.p.'s) of the atoms, that is indicative of static disorder. The phenomenon is particularly significant for the apical O atoms of the [NbO_6] octahedra (the mostly affected by the cooperative tilt) and for the Ba atoms hosted in the large pentagonal channels (that moves in the ab plane in agreement with the displacements of the apical O atoms lying on the same plane). Once the structural modulation is taken into account (at least partially) by refining these atoms on disordered positions, the triangular channels become able to host Pr^{3+} ions (Fig. 7).

Table 3. Selected bond lengths and distances (Å). Bonds denoted by a and b superscripts represents possible alternatives produced by the disordered description of the modulation in the fundamental cell.

	Pr:BNN (0.5%)	Pr:BNN (2%)	Pr:BNN (8%)
Nb2- O5	1.94(3)	1.92(2)	1.831(18)
Nb2- O1	4x1.958(4)	4x1.956(4)	4x1.958(4)
Nb2 -O5	2.08(3)	2.10(2)	2.179(18)
Nb1- O42[a]	1.830(17)	1.86(2)	1.870(19)
Nb1- O41[b]	1.88(2)	1.90(2)	1.88(2)
Nb1- O3	1.944(4)	1.945(4)	1.949(4)
Nb1- O1	1.960(4)	1.961(4)	1.953(3)
Nb1- O3	2.000(4)	1.997(4)	1.991(4)
Nb1- O2	2.004(2)	2.006(2)	2.005(2)
Nb1- O41[a]	2.15(2)	2.12(2)	2.14(2)
Nb1- O42[b]	2.181(18)	2.15(2)	2.138(19)
Na1(Pr1)-O3	4x2.655(10)	4x2.651(10)	4x2.657(12)
Na1(Pr1)-O41	4x2.688(11)	4x2.690(11)	4x2.698(10)
Na1(Pr1)-O42	4x2.777(12)	4x2.783(11)	4x2.761(10)
Pr2-O5	2.24(3)	2.31(4)	2.22(4)
Pr2-O41[a]	2x2.41(2)	2x2.37(2)	2x2.42(3)
Pr2-O42[b]	2x2.26(2)	2x2.22(2)	2x2.29(2)
Pr2-O1	2x2.53(2)	2x2.53(3)	2x2.34(5)
Pr2-O1	2x2.56(3)	2x2.59(3)	2x2.76(5)
Pr2-O2	2.65(3)	2.61(4)	2.53(5)
Pr2-O2	2.74(3)	2.72(4)	2.91(5)
Pr2-Nb (av.)	2.89(3)	2.91(4)	2.88(5)
Pr1-Nb (av.)	3.412(7)	3.412(8)	3.413(5)
Pr-Nb weighted av.	2.89(3)	3.18(2)	3.319(12)

Following this idea the occupancies of the extra-framework cations were refined in the final cycles, by constraining the total charge to compensate the anionic framework. The Pr^{3+} concentration of the most diluted crystal estimated by this approach significantly exceeds the nominal doping level and cannot be considered quantitatively reliable. Nevertheless these results allow concluding that in this sample praseodymium occupies the C site, compensating a small Ba deficiency in the A_2 site. The presence of some Pr^{3+} in the A_1 site of BNN:Pr (0.5%) cannot be excluded. However, being the refined occupancy of the order of the standard deviation, the Na occupancy of A_1 site was fixed to the unit in the last refinement cycles. The occupation of the C site by Pr is probably forced by the large Na excess in the flux that inhibits the competitor role of Pr for the A_1 site. As the doping level increases Pr^{3+} starts to occupy preferentially the A_1 site as usual for lanthanides in TTB structures, decreasing its occupancy in the C site. Refinement and atomic parameters are reported in Tables 1 and 2, respectively; selected bond lengths are reported in Table 3. In the Tables 2 and 3 we have indicated with Pr1 and Pr2 the Pr^{3+} ions located at the A_1 and C sites, respectively. The distribution of Pr^{3+} over the two sites influences the shortest Pr-Nb distance that represents a critical spectroscopic parameter. The average Pr-Nb shortest distance, determined for the three samples and weighted on the refined site occupancy (Table 3), is in good agreement with the values predicted from the spectroscopic behaviour, indicating the effectiveness of the proposed model.

5. Conclusions

The luminescence spectra of Pr:BNN crystals are influenced by the host properties and by the substitution mechanisms. Measurements as a function of the temperature, of the excitation wavelength and of the doping level have evidenced the presence of non equivalent optical centres whose emission properties are affected by different and concomitant non radiative processes. The interaction between host and doping ions results in the formation of an IVCT state that actively participates to the excited states dynamics of the system. In this context, the concentration shift of the IVCT band has been accounted for on the basis of a previously developed empirical model that allows formulating a hypothesis about the site occupancy of the Pr^{3+} ion in this host. The structures of the investigated materials have been determined by single crystal XRD measurements and are consistent with the supposed Pr^{3+} occupancy, and the connection with the growth procedure has been pointed out.

References

1. R. R. Neurgaonkar, W. K. Cory, *J. Opt. Soc. Am.* B **3** (1986) 274.
2. G. Foulon, A. Brenier, M. Ferriol, M. T. Cohen-Adad, G. Boulon, *Chem. Phys. Lett.* **249** (1996) 381.
3. A. Rodenas, D. Jaque, F. Agulló-Rueda, A.A. Kaminskii, *Opt. Comm.* **262** (2006) 220.
4. F. Carrillo-Romo, C. Goutaudier, Y. Guyot, M. T. Cohen-Adad, G. Boulon, K. Lebbou, A. Yoshikawa, T. Fukuda, *Opt. Mat.* **16** (2001) 199.
5. S. Bigotta, G. Gorini, A. Toncelli, M. Tonelli, E. Cavalli, E. Bovero, *Opt. Mat.* **28** (2006) 395.
6. S. Bigotta, A. Toncelli, M. Tonelli, E. Cavalli, E. Bovero, *Opt. Mat.* **30** (2006) 129.
7. S. Bigotta, M. Tonelli, E. Cavalli, J. *Phys.: Condens. Matter* **19** (2007) 476208.
8. E. Cavalli, A. Belletti, R. Mahiou, P. Boutinaud, *J. Lumin.* **130** (2010) 733
9. R. Naccache, F. Vetrone, A. Speghini, M. Bettinelli, J. A. Capobianco, *J. Phys. Chem. C* **112** (2008) 7750.
10. H. R. Xia, L. X. Li, H. Yu, X. L. Meng, L. Zhu, L. J. Hu, *Cryst. Res. Tech.* **34** (1999) 901.
11. M. Bettinelli, A. Speghini, A. Ródenas, P. Molina, M. O Ramírez, B. Capote, D. Jaque, L. E. Bausá, J. García Solé, *J. Lumin.* **122-123** (2007) 307.
12. P. Boutinaud, E. Cavalli, M. Bettinelli, *J. Phys. Condens. Matter* **19** (2007) 386230.
13. Nakazawa, E. *Phosphor Handbook*; CRC Press: Boca Raton, FL, 1999.
14. A. Altomare, M. C. Burla, M. Camalli, G. Cascarano, C. Giacovazzo, A. Guagliardi, A. G. G. Moliterni, G. Polidori, R. Spagna, *SIR2002, Program for Crystal Structure Solution and Refinement*; IRMEC-CNR, Bari, Italy, 2002.
15. G. M. Sheldrick, *SHELXL97, Program for Crystal Structure Refinement*; University of Gottingen, Germany, 1993.
16. P. B. Jamieson, S. C. Abrahams, J. L. Bernstein, *J. Chem. Phys*. **50** (1969) 4352.
17. P. Ju Lin, L. A. Bursill, *Acta Crystallogr. B* **43** *(*1987) 504.
18. P. Labbé, H. Leligny, B. Raveau, J. Scheck, J. C. Toledano, *J. Phys. Condens. Matter* **2** (1989) 25.
19. S. Fabbrici, E. Montanari, L. Righi, G. Calestani, A. Migliori, *Chem. Mater.* **16** (2004) 3007.

20. F. Mezzadri, S. Fabbrici, E. Montanari, L. Righi, G. Calestani, E. Gilioli, F. Bolzoni, and A. Migliori, *Phys. Rev. B* **78** (2008) 064111.